A Nonhydrostatic Mesoscale Simulation of the 10–11 June 1994 Coastally Trapped Wind Reversal

WILLIAM T. THOMPSON, TRACY HAACK, JAMES D. DOYLE, AND STEPHEN D. BURK

Marine Meteorology Division, Naval Research Laboratory, Monterey, California

(Manuscript received 29 October 1996, in final form 2 May 1997)

ABSTRACT

During the summer months, the California coast is under the influence of persistent northwesterly flow. Several times each summer, this regime is disrupted by coastally trapped wind reversals (CTWR) in which the northwesterly flow is replaced by southerlies in a narrow zone along the coast. Controversy exists as to the physical mechanisms responsible for initiation and maintenance of CTWRs. While it is clear that coastal terrain is important in creating the trapped response, the precise role played by terrain is unclear. In the present study, these issues are investigated using a nonhydrostatic mesoscale model to simulate the 10–11 June 1994 CTWR event. The results show that the model successfully reproduces many of the observed features of this event, including anomalous vertical structure involving the relatively shallow boundary layer with a warm, nearly neutral layer above; the northward propagation of southerly flow in advance of a tongue of coastal stratus/fog; and a substantial reduction in propagation speed due to the sea breeze. Of the several mechanisms that have been proposed in the literature to characterize these events, these results are most consistent with a topographically trapped gravity current. Further investigation, required to verify this hypothesis, is ongoing.

Two sensitivity studies are used to examine the role of terrain in producing and maintaining the CTWR. In the first sensitivity study, the coastline from Pt. Conception to Pt. Reyes is replaced with a straight line and a uniform 840-m-high ridge is placed adjacent to the coast. This simplification permits better isolation of the terrain influence on the mesoscale pressure field and the forcing of the CTWR by the pressure distribution. The results show that adiabatic warming associated with flow over the coastal terrain is required to produce the alongshore pressure gradient, which forces ageostrophic southerly flow, and that, in the absence of bays and gaps in this terrain, southerly flow extends to the location of the minimum pressure. In a second sensitivity study, the height of the ridge along the coast is set to zero. In this simulation there is no mesoscale organization of the southerly flow. Moreover, the structure of the marine boundary layer near the coast is altered by removal of downslope flow and the gravity current characteristics seen in the control and first sensitivity study are absent.

1. Introduction

During the summer months, the southwest coast of North America is often under the influence of the subtropical high over the eastern Pacific and a thermal trough over the southwestern United States. This results in persistent northwesterly flow along the coast that is strongly modulated by diurnal variations in coastal baroclinicity and topographic effects. Several times each summer this regime is disturbed by southerly surge events in which the northwesterly flow is replaced by southerlies in a narrow zone along the coast accompanied by significant near-surface cooling and development of stratus clouds. In strong cases, an abrupt shift to southerly flow with speeds of 15 m s^{-1} can occur along with rising pressure, cooling of 10°C or more, and a transition from clear to low overcast conditions (Mass and Albright 1987; hereafter referred to as MA87). Visible satellite imagery of these events is quite striking, showing a narrow tongue of stratus surging rapidly northward along the coast.

In the present study, we use a relatively high-resolution nonhydrostatic mesoscale model to simulate the coastally trapped wind reversal (CTWR) event of 10–11 June 1994. It should be noted that there have been no previous high-resolution simulations of such an event using real data. This simulation thus provides a unique opportunity to document details of the structure and evolution of a CTWR event. In a subsequent publication, we plan to perform an in-depth investigation of the dynamics of the CTWR. The emphases of the present study are to describe the simulation, validate the results against available observational data, and present preliminary findings on the impact of terrain on the CTWR.

One of the first studies of observational features of a CTWR is that of Dorman (1985), who noted that the CTWR displayed many of the features of a solitary trapped Kelvin wave. A detailed investigation of the 16–17 May 1985 event is given by MA87. In this case,

Corresponding author address: Dr. William T. Thompson, Naval Research Laboratory, Marine Meteorology Division, Monterey, CA 93943-5502.
E-mail: thompson@nrlmry.navy.mil

a sea level pressure (SLP) high initially located over British Columbia migrates to the southeast while the inverted thermal trough over southern California extends to the northwest and over the coast during the first 24 h. This creates an along-coast pressure gradient with lower pressure to the north. Southerly winds initially confined to the southern California Bight appear simultaneously along the coast from Pt. Conception to Monterey Bay about 6 h after the establishment of an along-coast pressure gradient. Southerly flow then propagates to the north with increasing speed from just north of Cape Mendocino to Tatoosh Island at the entrance to the Strait of Juan de Fuca. Southerly flow is confined to a narrow zone along the coast; the width of this zone is consistent with the Rossby radius of deformation. In this case and several more recent CTWR events, the southerly flow extends over a deep layer (3–5 km).

More recently, Ralph et al. (1995, 1996) have discussed the CTWR of 10–11 June 1994. The general structural features of the events described by MA87 and Ralph et al. are similar. However, some important differences are apparent. In the 1994 case, the surge did not extend north of Pt. Arena (about 200 km south of Cape Mendocino). Little variation in boundary layer structure with distance from the coast was apparent in this case as the depth was nearly horizontally uniform from at least 125 km west of the surge zone to the coast. Finally, while MA87 emphasize the role of lee troughing in the vicinity of high terrain along the northern coast in the 1985 event, Ralph et al. assert that horizontal warm air advection plays a dominant role in the 1994 CTWR event.

Observational and theoretical studies of these events suggest at least four mechanisms that may characterize CTWR events. Recently, there have also been suggestions that some combination of these mechanisms may be involved (Reason and Steyn 1992). These mechanisms consist of the ageostrophic mesoscale response to along-coast pressure gradients produced by the orography and the synoptic-scale flow (Mass et al. 1986; MA87; Mass and Bond 1996), a mesoscale response to a frictionally induced potential vorticity anomaly (Persson et al. 1995, 1996), a Kelvin wave response (Dorman 1985); Rogerson and Samelson 1995), and a topographically trapped gravity current response (Dorman 1987; Klemp et al. 1994; MA87).

The mesoscale response to an along-coast pressure gradient relies on synoptic-scale forcing producing lower surface pressures in the lee of the coastal mountains of northern California. Heating due to offshore flow results in low-level troughing along the coast. Flow near the coast is unable to attain geostrophic balance within a Rossby radius of deformation ($\sim$80 km) of the coast due to the presence of blocking terrain and thus flows ageostrophically down the pressure gradient toward the north.

Recently, Persson et al. (1995, 1996) have suggested that southerly flow associated with the CTWR is induced by a low-level plume of potential vorticity (PV) emanating from the steep terrain north of San Francisco. Potential vorticity is generated by friction as flow with an offshore component interacts with the steep terrain. The maximum PV anomaly lies within the inversion above the marine boundary layer; thus the southerly flow attributable to the PV need not be confined to the boundary layer.

The Kelvin wave response is hypothesized to be initiated by preferential lifting of the top of the marine boundary layer (MBL) to the south along the coast. A Kelvin wave requires the existence of a wall (in this case, the coastal terrain) to the right of the flow (in the Northern Hemisphere). This response consists of a wavelike disturbance that propagates along the interface between a dense layer below (the MBL) and a less dense layer above (the overlying atmosphere, which is assumed to remain quiescent during the event). This produces a positive surface pressure perturbation resulting from variations in the depth of the boundary layer. The amplitude of the wave decays exponentially away from the wall with an *e*-folding distance equal to the Rossby radius of deformation. The origin of the preferential lifting of the top of the MBL that initiates the event is unclear.

The topographically trapped gravity current response is based on the assumption that a deep, cool MBL exists to the south with a shallow or nonexistent boundary layer to the north. The deep MBL to the south acts as a reservoir of dense fluid, which is released and flows northward to displace the less dense fluid. This response differs from a Kelvin wave in that there is a discontinuity (in both potential temperature and vertical motion) across a gravity current head that does not exist for a Kelvin wave. There is also considerable small-scale vertical motion in the vicinity of a gravity current head. The mechanism responsible for releasing the gravity current and allowing flow to the north is not well understood. There have been suggestions in the literature that Kelvin waves may evolve through nonlinear processes into a feature resembling a gravity current (Klemp et al. 1994; Rogerson and Samelson 1995; Reason and Steyn 1992). Thus, a Kelvin wave may be the mechanism that releases the gravity current.

A key feature in all of the proposed mechanisms is the influence of terrain. MA87 and Mass and Albright (1989) provide discussion of the dynamics of flow near a barrier in support of the trapped ageostrophic response as well as implicating the terrain of northern California in initiating the CTWR. In all of the arguments in favor of both the Kelvin wave and gravity current responses involving a two-layer fluid, the existence of a wall to the right of the flow is required.

We investigate the impact of terrain on the 10–11 June 1994 CTWR event herein using the Naval Research Laboratory's Coupled Ocean/Atmosphere Mesoscale Prediction System (COAMPS) nonhydrostatic model (Hodur 1997). Through a detailed analysis of a control

simulation, we demonstrate that the model successfully reproduces many of the observed features of this event. We also perform sensitivity studies involving modifications to the terrain height field. In section 2, we describe the model and model implementation for the current study. In section 3, we provide a description of the 10–11 June event. Section 4 is devoted to a detailed description of the results of the control simulation and model validation against available data. Section 5 describes the results from two sensitivity studies. We review the results and discuss our conclusions in section 6.

2. Model description

COAMPS is a three-dimensional, fully compressible, nonhydrostatic model based upon the work of Klemp and Wilhelmson (1978). Only the atmospheric portion of COAMPS is utilized for the present study. As described by Hodur (1997), it consists of eleven prognostic equations: three momentum equations, the pressure and thermodynamic equations, five moisture equations, and a subgrid-scale turbulent kinetic energy (TKE) equation. A time-splitting technique allows for a computationally efficient method of integrating these equations. The fast modes (acoustic waves) are computed semi-implicitly by separating them from terms involving the advective modes. Gravity waves are treated using a split-explicit technique. Here, we briefly highlight the physical parameterization schemes that play the most significant roles in the simulation of the CTWR.

In parameterizing boundary layer processes, COAMPS uses a prognostic equation for TKE that is based on the Mellor and Yamada (1982) level 2.5 formulation. Counter gradient correction terms are included for the potential temperature and water vapor equations (Therry and LaCarrere 1983). Eddy mixing coefficients for scalars and momentum are related by a proportionality constant and depend upon the flux Richardson number, TKE, and turbulent length scale l, which is based on the Blackadar (1962) formulation. The asymptotic limit of l is dependent upon the ratio of the zeroth to the first moments of the vertical distribution of turbulent kinetic energy modulated by a stability-dependent parameter (Thompson and Burk 1991). Horizontal mixing of the prognostic variables is based upon the horizontal deformation fields as described by Smagorinsky (1963).

The surface fluxes are computed from the Louis et al. (1979) formulation. This scheme uses Monin–Obukhov similarity theory and the flux-profile relationships of Businger et al. (1971) with Richardson number–dependent functions for the exchange coefficients. The surface fluxes and surface radiation contributions are incorporated into a surface energy budget based on the force–restore method of Deardorff (1978). In this approach, forcing due to surface heat and moisture fluxes and the net radiative flux are combined with a restore term that drives the surface temperature toward the climatological deep soil temperature with a specified time constant. This methodology allows the model to develop a fairly realistic diurnal surface temperature wave without the necessity of a multiple soil layer model. The combined effects of long- and shortwave radiation are parameterized following Harshvardhan et al. (1987) with additional details provided in Hogan and Rosmond (1991).

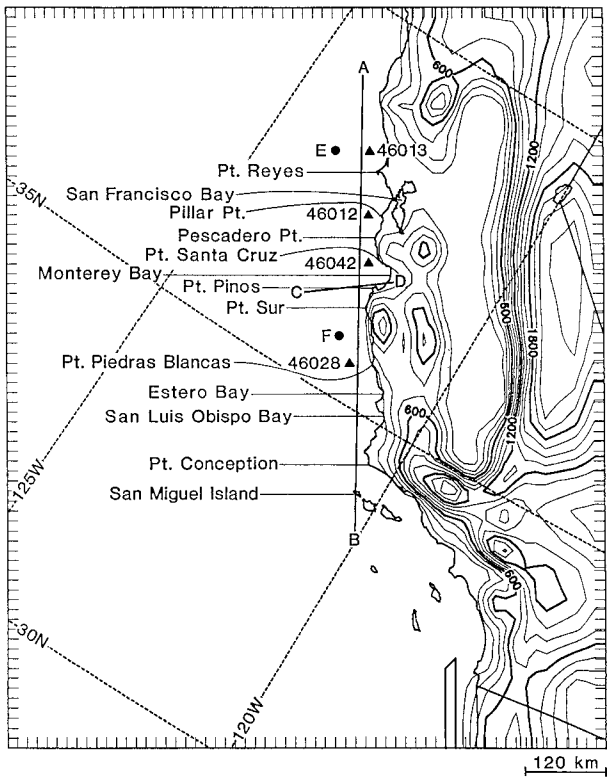

FIG. 1. Map showing model 15-km mesh terrain height field (m) and locations referenced in text. Contour interval is 150 m.

The cloud microphysics scheme is based on Rutledge and Hobbs (1983). This scheme features prognostic equations (continuity equations) for the mixing ratios of the following five water substance species: water vapor q_v, cloud water q_c, rain q_r, cloud ice q_i, and snow q_s. Source and sink terms in these prognostic equations are specified in terms of 13 different microphysical conversion processes. In the present study, the ability of the scheme to represent marine fog and stratus is evaluated.

The domain configuration used to simulate the June 1994 CTWR event includes two horizontally nested grids oriented parallel to the California coast with 45-km and 15-km grid spacing, respectively. These two nests are shown in Figs. 1 (15-km mesh) and 2 (45-km mesh). The model depth extends to 30 km and comprises 30 levels with vertical resolution ranging from 20 m near the surface to 7.5 km at the top. The advective mode time step is 120 s and the acoustic mode time step is 60 s.

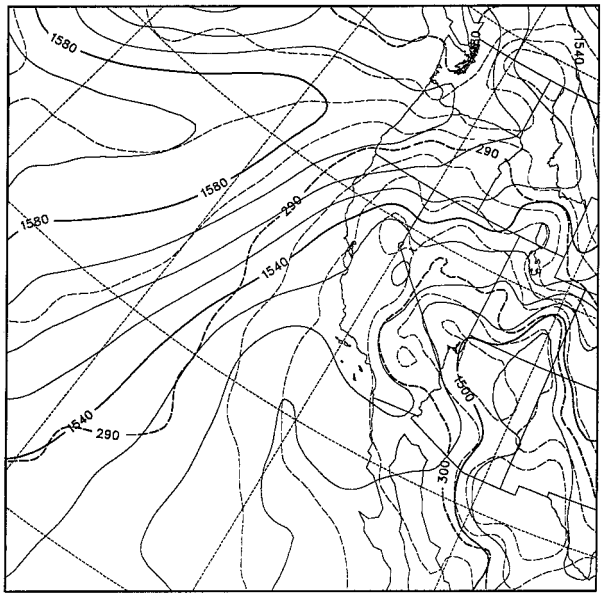

FIG. 2. The 850-mb height (m) and temperature (K) analyses valid 0000 UTC 10 June 1994 from the 45-km mesh. Contour intervals are 10 m and 2.5 K.

A 36-h COAMPS simulation, beginning 0000 UTC (1700 local time) 10 June 1994, is initiated using an incremental update data assimilation procedure that allows for the retention of mesoscale detail in the initialized fields. This procedure begins with a 12-h preforecast beginning at 0000 UTC 9 June 1994 using first-guess fields from the Navy's global model (NOGAPS) modified by an optimum interpolation (OI) analysis. This OI procedure is performed on each of the two grids. That 12-h COAMPS preforecast provides first guess fields, updated with current OI increments, for a second 12-h preforecast. The second preforecast provides the first-guess fields for the simulation study period. During both the preforecast and the simulation, time-dependent lateral boundary conditions are obtained from NOGAPS forecast fields every 12 h.

3. The CTWR event of 10–11 June 1994

a. Synoptic-scale features

A detailed description of the synoptic-scale evolution of this event is given by Ralph et al. (1995, 1996). Here, we will highlight only features having a direct bearing on the present study. Shown in Fig. 2 is an analysis of the 850-mb heights and temperatures from the 45-km mesh valid at 0000 UTC 10 June. At this level, there is a strong ridge over the Pacific Northwest imparting an easterly (offshore) geostrophic component to the general northerly flow along the coast. These features are also present at 700 mb. Examination of the temperature distribution shows that anomalously warm temperatures extend as far north as central Oregon and significant warm advection is present over the Northern California coast. Assuming hydrostatic balance, Ralph et al. (1995) attributed an approximately 3–4-mb surface pressure decrease in this region to warm advection. As the upper-level ridge drifts to the east, southerly flow is established over a deep layer; large scale, quasigeostrophic southerly flow extends to 6 km in this case.

Many of the features evident at 850 mb are reflected at the surface. In particular, a surface high is present over the Pacific Northwest. Strong offshore flow is occurring over central California, resulting in ''heat wave'' conditions at coastal locations (e.g., the high temperature on 11 June at San Francisco was 36°C, 17°C above the monthly mean maximum temperature). Many CTWR events are preceded by heat wave conditions. In conjunction with high temperatures at coastal locations, the thermal trough initially over central California drifts to the west. By 1800 UTC 10 June, it is centered over the coast, extending north from Pt. Conception to central Oregon (Oosterling 1995). Offshore flow is replaced by southerly flow along the coast with the transition moving to the north with time. Southerly flow at the surface lags southerly flow at upper levels by 2–3 h. A surface cold front appears in the National Weather Service analyses off the coast of Oregon by 1200 UTC 11 June. By 1200 UTC 12 June, the surface cold front is located between San Francicso and Monterey.

b. Mesoscale features

Special mesoscale observations of the June 1994 event were collected under the auspices of the Coastal Meteorology Accelerated Research Initiative sponsored by the Office of Naval Research. These observations are documented and analyzed by Ralph et al. (1995, 1996).

The CTWR is initiated with weak southerly flow in the Santa Barbara Channel at 0600 UTC 10 June and ends between 1200 UTC 11 June and 0000 UTC 12 June. The leading edge of the southerlies passes Pt. Conception between 1200 and 1400 UTC 10 June. Southerly flow extends to Monterey Bay by 1700 UTC (as indicated by the wind reversal at buoy 46042; see Fig. 1) and to Pt. Reyes (buoy 46013) by 1100 UTC 11 June. Southerly flow does not extend to Pt. Arena. The strongest southerly wind is 8 m s^{-1}, and the southerlies propagate to the north with a phase speed of 10–11 m s^{-1} (Ralph et al. 1996), although propagation is substantially impeded by the sea breeze in the vicinity of Monterey Bay. This topic will be addressed below.

A surge of coastal stratus was observed in satellite imagery. A series of visible satellite images valid at 1618 and 1810 UTC 10 June and 0122 11 June is shown in Figs. 3a–c. Low cloudiness, initially confined to the southern California Bight, extends to Pt. Piedras Blancas 1600 UTC 10 June. Clouds extend to Pt. Sur by 1800 UTC 10 June and enter Monterey Bay by 0000 UTC 11 June. Clouds extend north of San Francisco Bay by

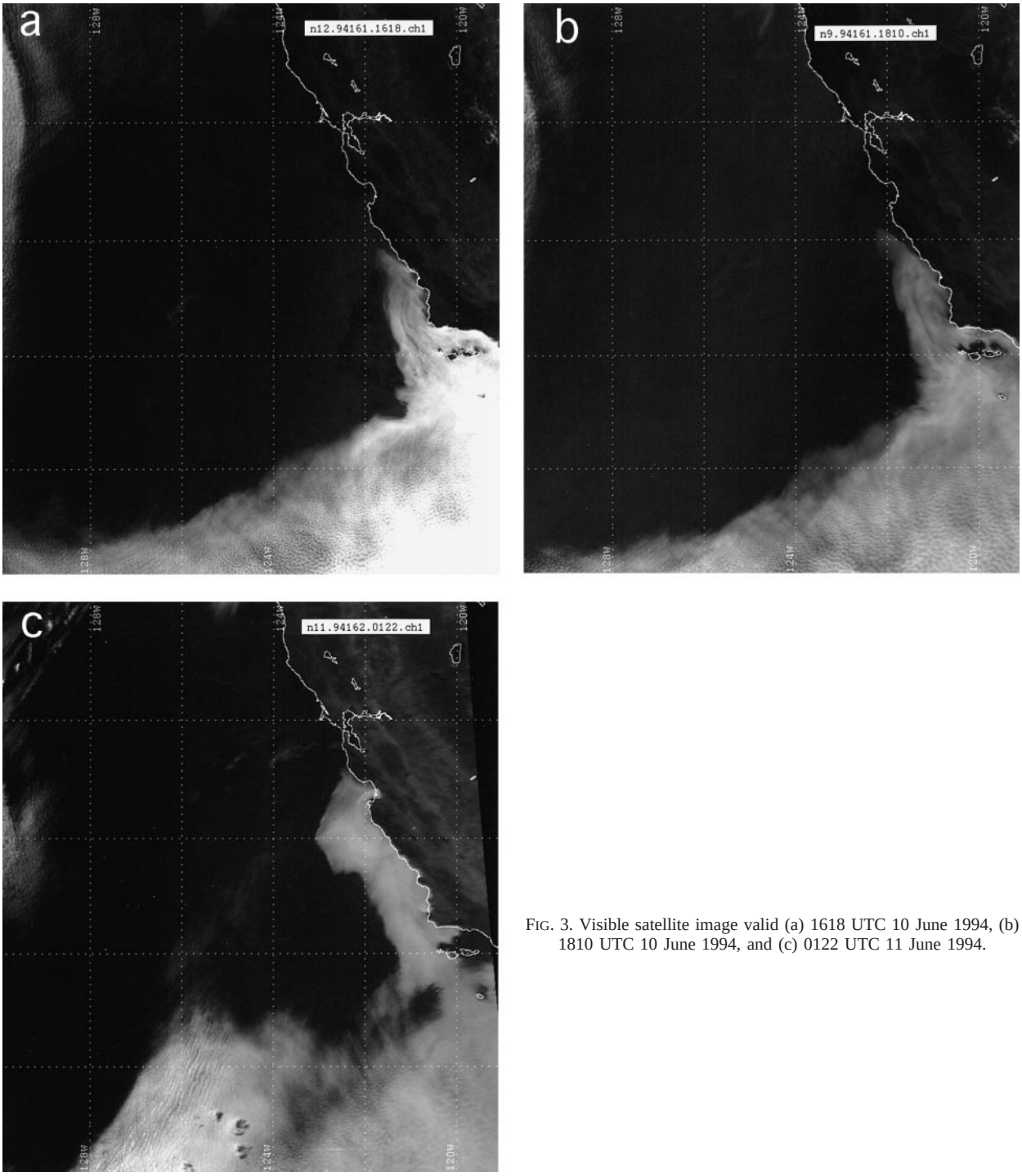

FIG. 3. Visible satellite image valid (a) 1618 UTC 10 June 1994, (b) 1810 UTC 10 June 1994, and (c) 0122 UTC 11 June 1994.

1500 UTC 11 June. Observations from a research vessel indicate that the arrival of southerly winds precedes the arrival of stratus by as much as 3 h. By 1200 UTC 11 June, the stratus extends well to the west of the narrow zone of southerly flow along the coast.

Mesoscale pressure analyses for this event indicate that a narrow ridge forms seaward of the coastline as the CTWR propagates to the north (Ralph et al. 1996). The strongest southerly winds are coincident with the ridge and increase in strength as the along-coast pressure gradient at the leading edge of the ridge increases. A low pressure area centered 200 km west of Pt. Conception is present in the analysis for 1800 UTC 10 June. The strength of the along-coast pressure gradient in-

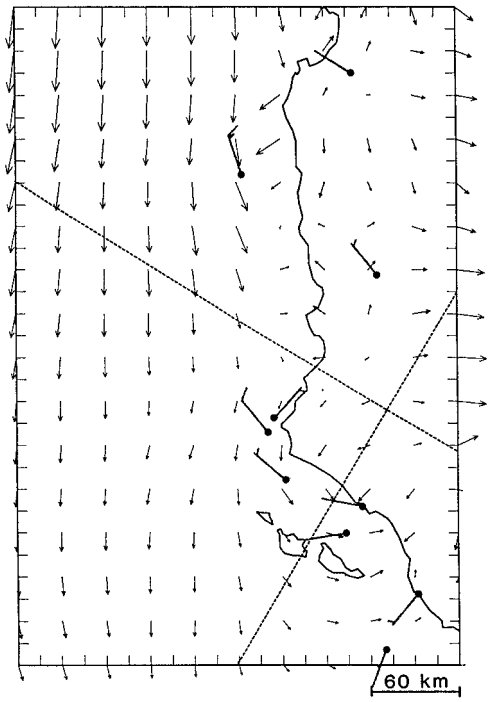

FIG. 4. Model forecast 10-m wind field and observed wind barbs for the 6-h forecast valid 0600 UTC 10 June 1994. Only a portion of the model 15-km domain is shown (note the scale in Fig. 4). The largest vectors correspond to 10 m s^{-1} and the wind barbs correspond to 5 m s^{-1} (half-barbs are increments of 2.5 m s^{-1}).

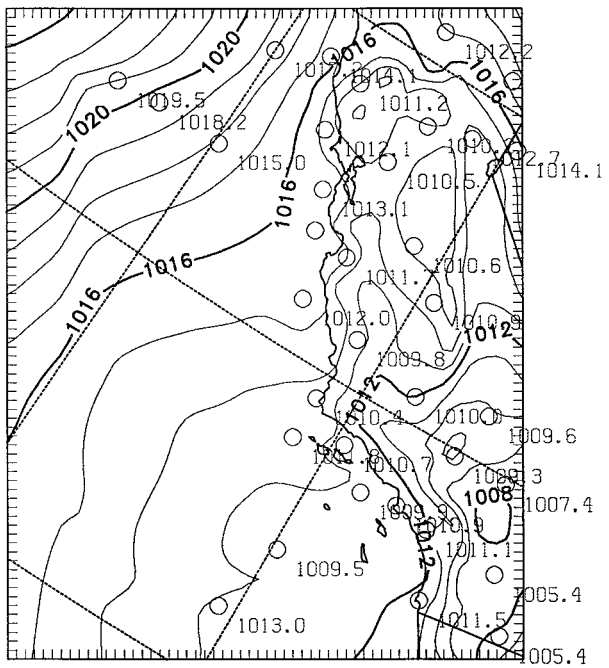

FIG. 5. Model sea level pressure distribution (mb) and observed pressures for initial time valid 0000 UTC 10 June 1994. Contour interval is 1 mb. The pressure observation locations are indicated by an open circle slightly above and to the left of the plotted value.

creases in time with the pressure at Pt. Reyes 2.1 mb lower than the pressure at Pt. Conception at 0000 UTC 11 June.

4. Validation of the COAMPS model simulation of the 10–11 June CTWR event

a. Wind and mass field evolution

1) PREINITIATION PHASE

The 36-h COAMPS simulation begins at 0000 UTC (1700 local time) 10 June 1994. At this time, winds are northerly along the coast becoming westerly in the southern California Bight. The model 10-m wind vectors for 0600 UTC (2300 LT) 10 June are shown in Fig. 4 (only a portion of the model 15-km domain is shown). Observed wind barbs are superimposed on the model wind field. Note that the observations and model indicate significant cyclonic shear in the Santa Barbara Channel and that the model flow is offshore along the coast south of Monterey Bay.

The initial SLP field valid at 0000 UTC 10 June is shown in Fig. 5 along with the observed pressure. The primary features of the pressure field include a pronounced heat trough in the Central and Sacramento Valleys, the strong pressure gradient over the northeast Pacific, and the relatively weak pressure gradient over

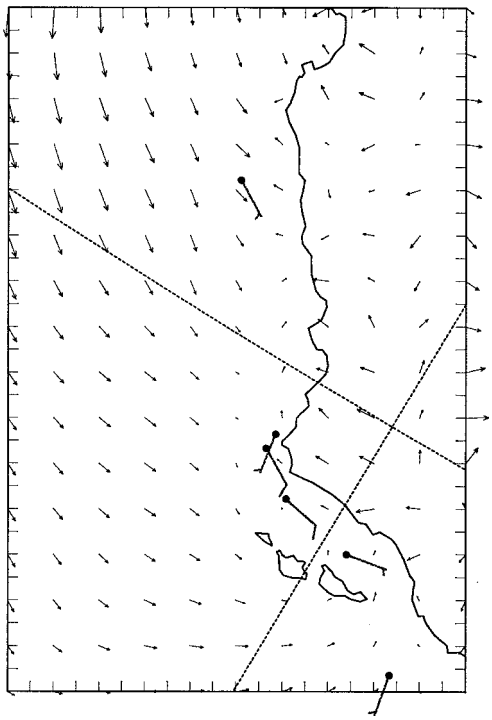

FIG. 6. As in Fig. 4 except for 14-h forecast valid 1400 UTC 10 June 1994.

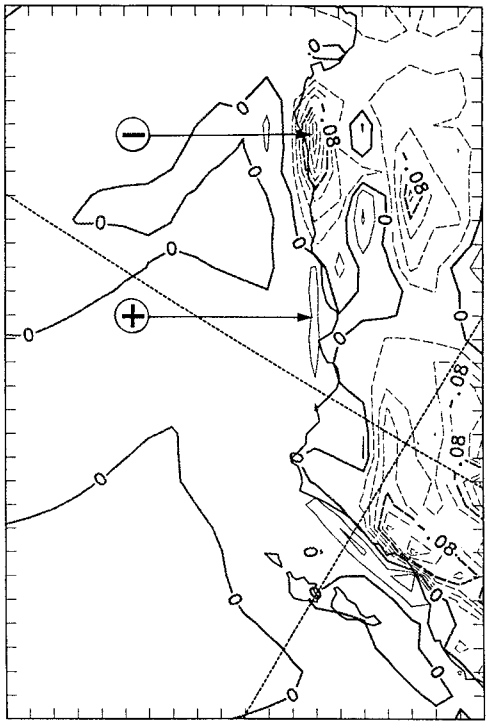

FIG. 7. Model forecast 950-mb vertical motion field (m s^{-1}) valid 1400 UTC 10 June 1994. Contour interval is 0.02 m s^{-1}. Dashed contours indicate downward motion.

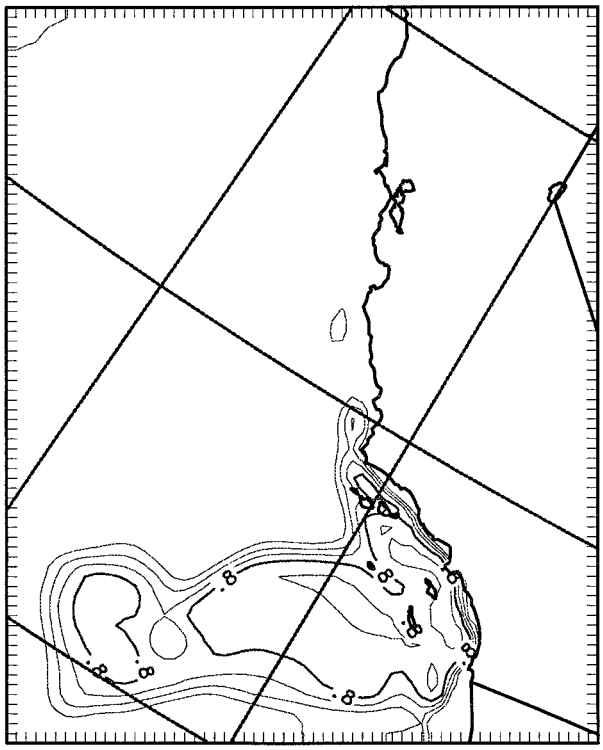

FIG. 9. Model 16-h forecast 10-m cloud liquid water mixing ratio (g kg^{-1}) valid 1600 UTC 10 June 1994. Contour interval is 0.2 g kg^{-1}.

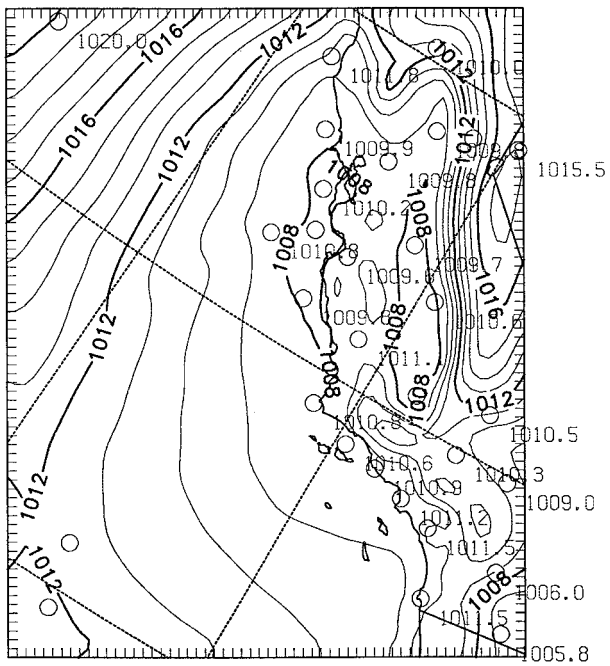

FIG. 8. As in Fig. 5 except for 12-h forecast valid 1200 UTC 10 June 1994.

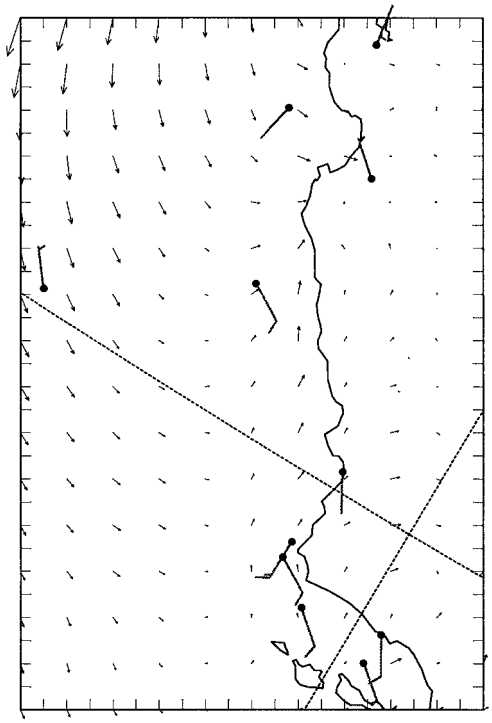

FIG. 10. As in Fig. 4 except for 18-h forecast valid 1800 UTC 10 June 1994.

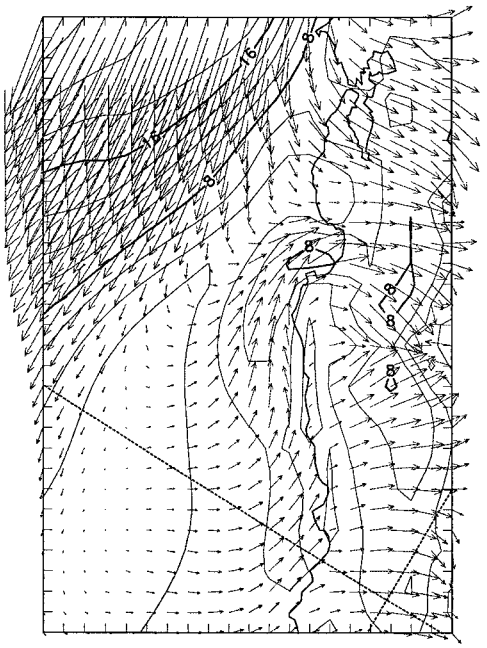

FIG. 11. Model forecast 990-mb wind vectors and isotachs (m s^{-1}) valid 0000 UTC 11 June 1994. Contour interval is 2 m s^{-1}.

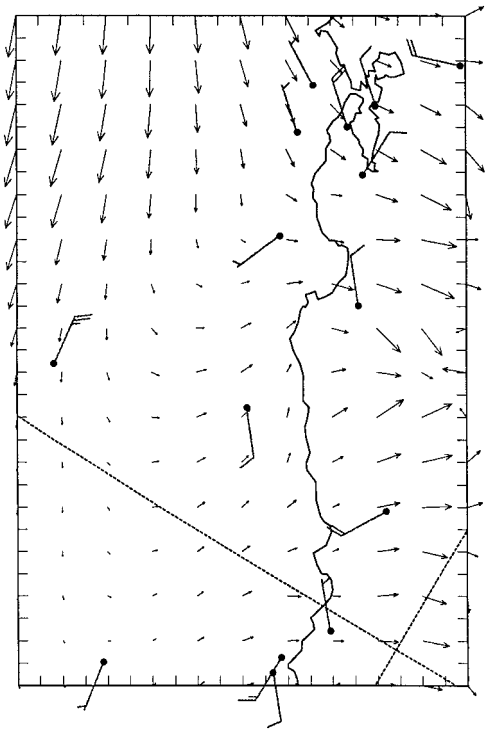

FIG. 12. As in Fig. 4 except for 24-h forecast valid 0000 UTC 11 June 1994.

coastal southern and central California. Close agreement exists between the observed and modeled pressure distributions.

2) INITIATION PHASE

Southerly flow first appears north of Pt. Conception at 1300 UTC 10 June. The model 14-h forecast 10-m wind field valid at 1400 UTC (0700 LT) is shown in Fig. 6 along with the observed wind barbs. At this time, southerly flow extends to Pt. Piedras Blancas and has a large easterly component, in agreement with the observation from buoy 46028.

At 1400 UTC, the vertical motion field at 950 mb shows downslope flow near Pt. Sur extending offshore with a narrow tongue of ascending motion in the region of southerly flow (Fig. 7). Ascent is also occurring along the coast within the southern California Bight.

The forecast SLP distribution for 1200 UTC is shown in Fig. 8. Note that the along-coast pressure gradient is in agreement with the observations. The model pressure distribution is in good agreement over the ocean, whereas the observed pressure over land is 1–2 mb higher than that in the model. Pressures have fallen both along the coast and offshore over the previous 12 h, in agreement with observed tendencies. The lowest simulated pressure along the coast (1007.2 mb) is just to the south of Monterey Bay and a weak pressure ridge is apparent along the coast south of Pt. Conception. The pressure ridge along the coast is a common feature in CTWR events (MA87).

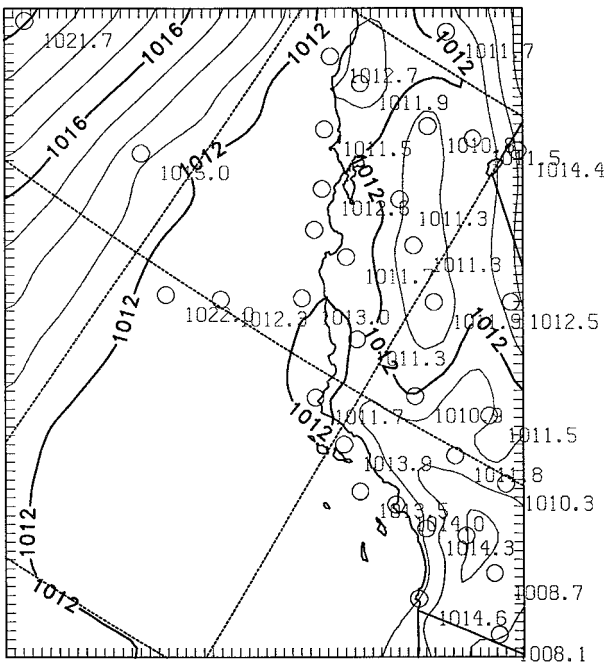

FIG. 13. As in Fig. 5 except for 18-h forecast valid 1800 UTC 10 June 1994.

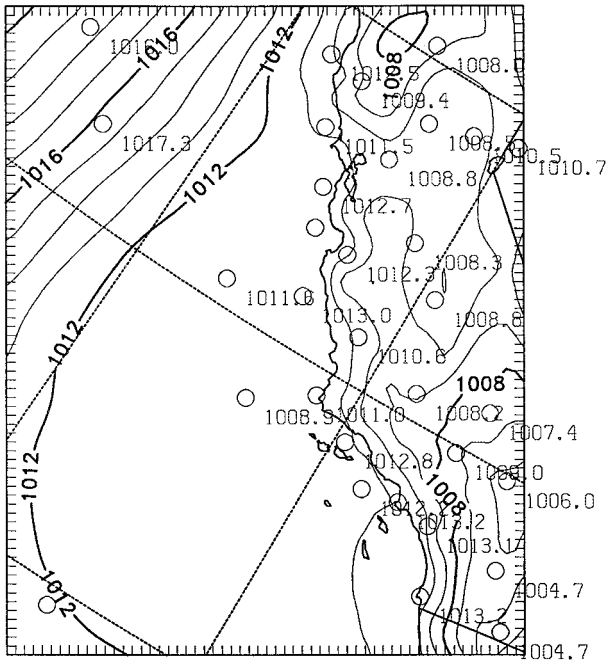

FIG. 14. As in Fig. 5 except for 24-h forecast valid 0000 UTC 11 June 1994.

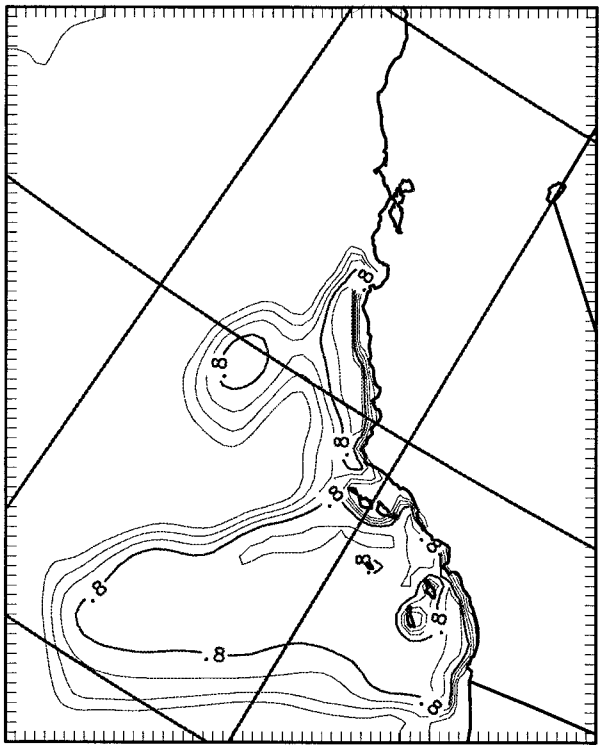

FIG. 16. As in Fig. 9 except for 24-h forecast valid 0000 UTC 11 June 1994.

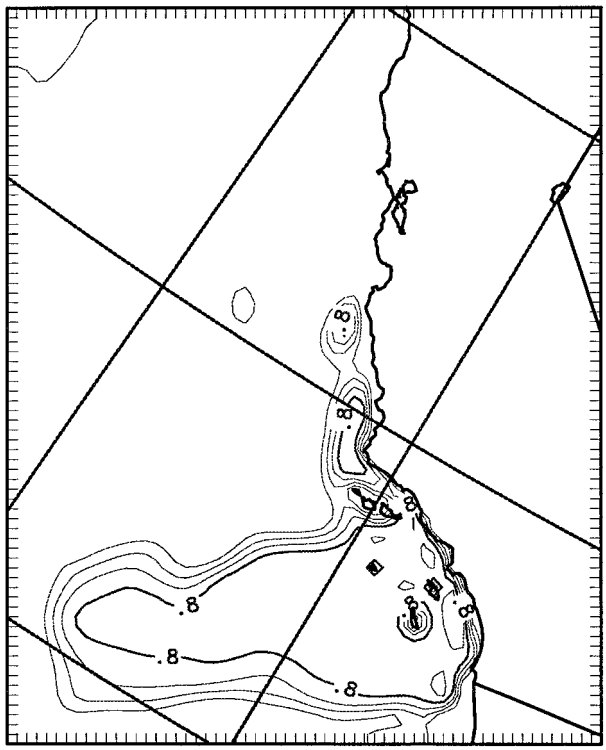

FIG. 15. As in Fig. 9 except for 18-h forecast valid 1800 UTC 10 June 1994.

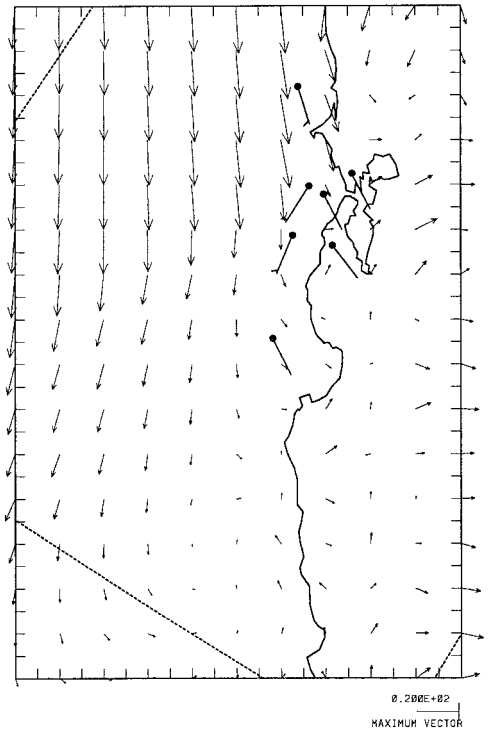

FIG. 17. As in Fig. 4 except for 36-h forecast valid 1200 UTC 11 June 1994. Here, the largest vectors correspond to 20 m s^{-1}.

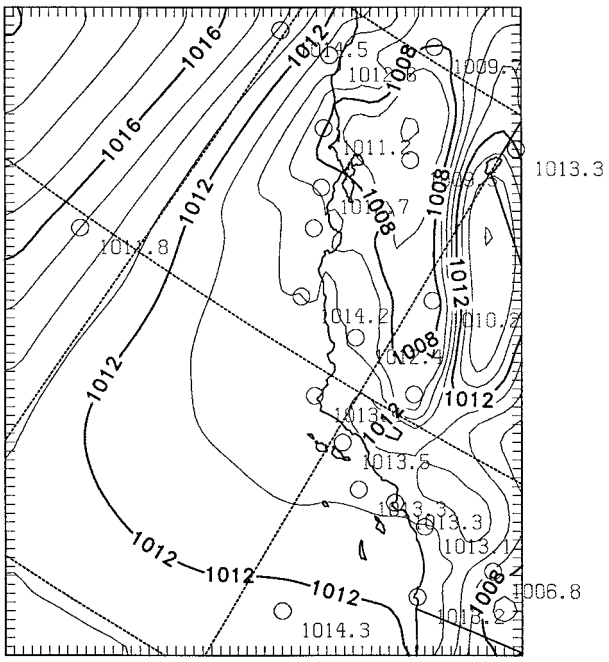

FIG. 18. As in Fig. 5 except for 36-h forecast valid 1200 UTC 11 June 1994.

Detailed examination of the model SLP distribution shows that a small-scale (~75 km) low pressure center, initially located just to the south of Pt. Sur, propagates steadily to the north from 1000 to 1600 UTC 10 June. From 1200 to 1500 UTC, a relatively uniform along-coast pressure gradient extends to the south from Pt. Sur to Pt. Conception. By 1600 UTC, the along-coast pressure gradient contracts and is concentrated near Pt. Sur as a mesoscale pressure ridge begins to advance to the north with a ''tongue'' of fog/stratus.

The 10-m level 16-h forecast cloud water field at 1600 UTC is shown in Fig. 9 (a visible satellite image for 1618 UTC 10 June is shown in Fig. 3a). The model cloud field agrees with the satellite imagery consistently though the simulation; a satellite image near 1400 UTC is quite similar to the model forecast cloud water distribution for 1400 UTC (not shown). Analysis of the model output indicates that the arrival of southerly flow precedes the arrival of low clouds by approximately 3 h, as documented by Ralph et al. (1995).

3) MATURE PHASE

At 1700 UTC, the model forecast low-level southerly flow enters Monterey Bay. Southerly flow at this time is confined to a region near the coast on the south side of the Bay and is not consistent with buoy 46042, which is reporting southerly flow just to the north and west of the Bay. The model forecast near-surface wind field at 1800 UTC is shown in Fig. 10. There is a broad (~75 km wide) band of strong southeasterly (coast parallel) wind extending along the coast from Pt. Conception to Pt. Pinos, in agreement with the observations. Within Monterey Bay, the westerly component of the wind has increased substantially with the onset of the sea breeze, although there is weak southerly flow at a height of about 100 m on the south side of the Bay.

Between 1700 10 June and 0000 UTC 11 June, there is evidence of a southerly low-level jet extending up the coast from San Luis Obispo Bay to Monterey Bay. The jet is most well defined within the inversion capping the marine boundary layer at the 990-mb level. The model forecast 990-mb wind vectors with isotachs are shown for 0000 UTC 11 June in Fig. 11. The model forecast 10-m winds for 0000 UTC 11 June are show in Fig. 12. At this level, southerlies extend to Pt. Sur, while 120 m above the surface, strong southerly flow continues just beyond Monterey Bay.

In both the observations and the simulation, propagation of the CTWR is substantially slowed in the vi-

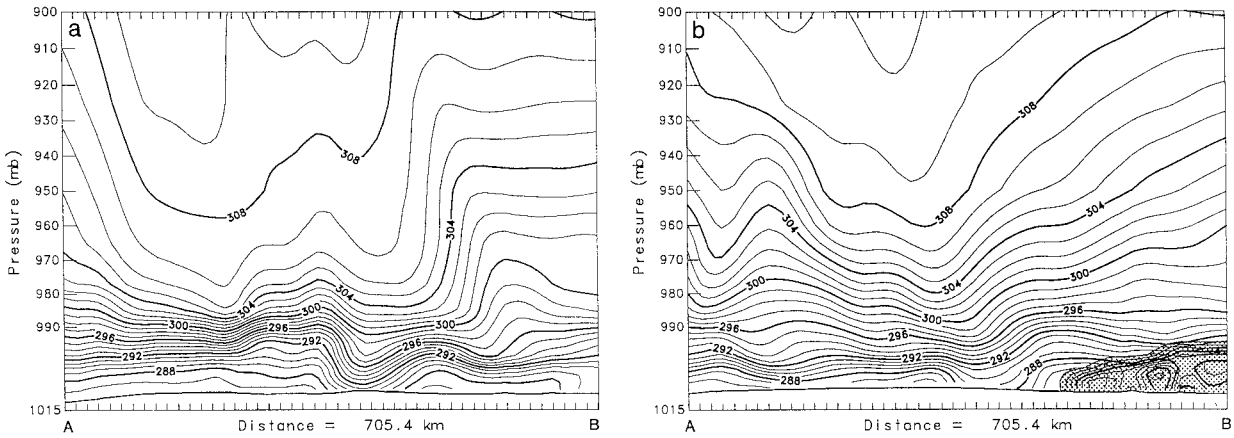

FIG. 19. Model forecast cross section of potential temperature (K) and cloud liquid water mixing ratio (g kg^{-1}; shaded). The plane of the cross section, *AB*, is shown in Fig. 1. Contour interval is 1 K. (a) The 6-h forecast valid 0600 UTC 10 June 1994. (b) The 18-h forecast valid 1800 UTC 10 June 1994.

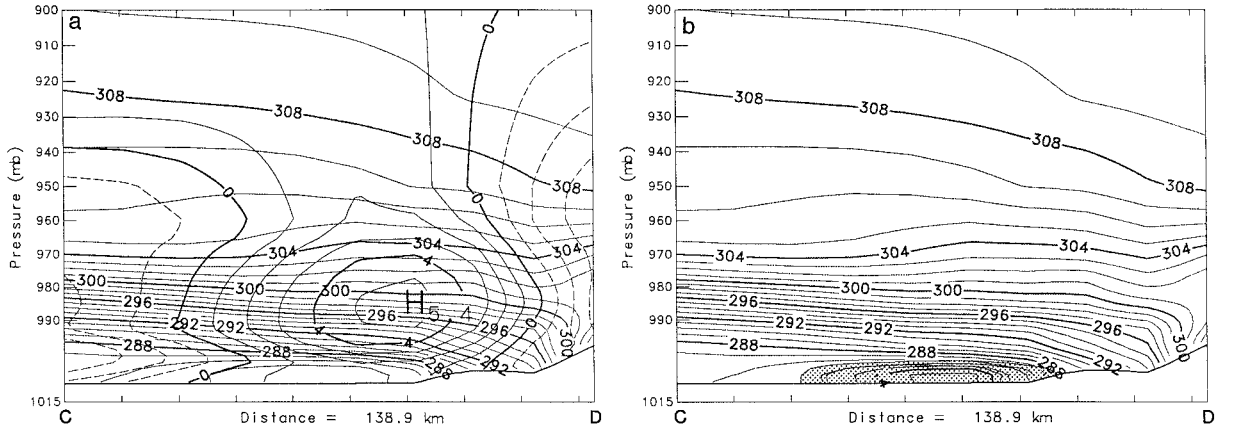

FIG. 20. Model forecast cross section valid 2200 UTC 10 June 1994. The plane of the cross section, *CD,* is shown in Fig. 1. (a) Potential temperature (K) and wind component normal to the cross-sectional plane (m s^{-1}; positive values represent south-southeasterly flow and negative values indicate north-northwesterly winds); contour intervals are 1 K and 1 m s^{-1}. (b) Potential temperature (K) and cloud liquid water mixing ratio (shaded).

cinity of Monterey Bay due to the sea breeze. In their climatological study, Bond et al. (1996) found that flow reversals (from northerly to southerly) were rare along this section of the coast in the afternoon due to diurnal modulation of the sea breeze. In the observations, the rate at which the flow reversal progresses up the coast drops from approximately 11 to 1.5 m s^{-1} after reaching Monterey Bay during the late afternoon. In the model simulation, the rate of propagation of the CTWR up the coast drops from 11 to 1.6 m s^{-1} during the same period.

At 1800 UTC, the vertical motion field (not shown) has a maximum of 0.08 m s^{-1} at 950 mb near Pt. Sur where the southerly flow begins to turn anticyclonically. The maximum ascent appears at the leading edge of the isotach maximum at this time. The vertical motion field at 0000 UTC 11 June shows ascent along the coast from south of Pt. Conception to south of San Francisco Bay as onshore flow impinges on the steep coastal terrain.

At 1800 UTC, the lowest pressure along the coast is 1011.6 mb over Pt. Reyes (Fig. 13), in excellent agreement with buoy 46013 (1011.5), and the along-coast pressure gradient extending from Pt. Piedras Blancas is much stronger than it was at 1200 UTC (Fig. 8). The model pressure distribution is in good agreement with the plotted observations and features a mesoscale ridge along the coast from Pt. Conception to north of Pt. Piedras Blancas and a broad trough extending from the north coast. The analysis from Oosterling (1995) for this time indicates a sharp open trough, in general agreement with the model simulation.

Shown in Fig. 14 is the SLP distribution for hour 24. The SLP distribution shares many features with the analysis from Ralph et al. (1996) including the low pressure off the coast near Pt. Conception and the increasing along-coast gradient to the north. A high-resolution analysis of model output (not shown) reveals a weak mesoscale ridge along the coast from Pt. Conception to Monterey Bay and a weak, elongated closed low off the coast near Pt. Conception. The analyses of Ralph et al. and Oosterling (1995) at this time are in agreement with the model as to the existence of a small-scale low centered approximately 200 km offshore near Pt. Conception.

Figure 15 shows the model cloud water field at 1800 UTC (a visible satellite image for 1810 UTC 10 June is shown in Fig. 3b). At this time, clouds extend to Pt. Sur and the model and satellite image agree in that the northern portion of the cloud tongue is 15–20 km offshore. The model 24-h forecast cloud water field valid at 0000 UTC 11 June is shown in Fig. 16 (the satellite image for 0122 UTC 11 June is shown in Fig. 3c). Both the model and the satellite show clouds entering Monterey Bay and extending to the north of the bay as well with an increase in the width of the cloud tongue south of Monterey. The clouds were observed to extend into the northwesterly flow. The westward extent of the cloudiness in the model is somewhat greater than observed, however.

4) DECAY PHASE

The model 10-m wind field for 1200 UTC 11 June (0500 local) is shown in Fig. 17 along with the observed wind barbs. Strong northwesterly flow extends southwest from Pt. Reyes, impeding the progress of the southerly flow north of Monterey Bay at this level. The observations, in contrast, show southerly flow extending to Pt. Reyes. However, at 1000 mb, southerly flow reaches its farthest northward progression in the model (about 100 km south of Pt. Reyes) at hour 30.

The SLP distribution for 1200 UTC 11 June is shown in Fig. 18. At this time, a mesoscale pressure trough extends offshore from Pt. Reyes and a weak mesoscale ridge is present near Pt. Sur. The analysis from Oosterling (1995) also depicts a trough extending from north of San Francisco.

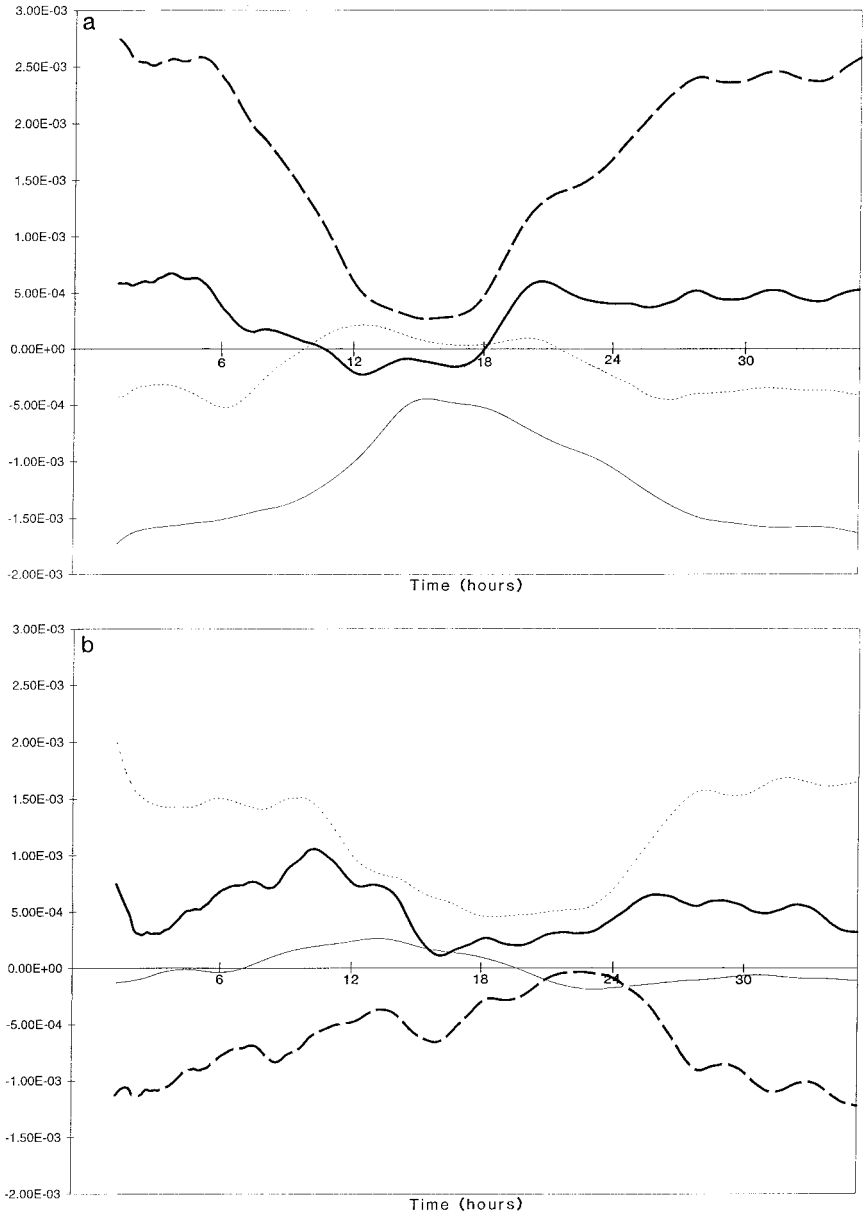

FIG. 21. Time series of the components of the momentum budget at 55 m: total acceleration (heavy solid line); pressure gradient (heavy dashed line); Coriolis (light solid line); and diffusion (dotted line) (see text for details). Plotted on the ordinate is the acceleration in units of meters per second per model time step where the model time step is 120 s. See Fig. 1 for locations: (a) across-coast momentum at point *E* (near Pt. Reyes), (b) along-coast momentum at point *E*, (c) across-coast momentum at point *F* (south of Pt. Sur), (d) along-coast momentum at point *F*.

b. Boundary layer evolution

Figure 19a shows a vertical cross section of the 6-h forecast potential temperature along the coast from just north of Pt. Reyes to just south of San Miguel Island and from the surface to 900 mb valid at 0600 UTC 10 June (the plane of the cross section is shown in Fig. 1). Note the shallow MBL topped by a strong inversion; the homogeneous nearly neutral, and very warm layer extending from the inversion to about 900 mb over the northern two-thirds of the cross section; and the region of closely spaced, nearly vertical isentropes south of the homogeneous, nearly neutral layer. This vertical structure is in contrast with the typical summertime MBL, which tends to be deeper with a weaker inversion and a cooler overlying layer. The unusually warm conditions above the inversion are the result of warm advection associated with offshore flow. Coastal sites were also anomalously warm.

A potential temperature vertical cross section valid at 1800 UTC is shown in Fig. 19b. Note the relatively deep,

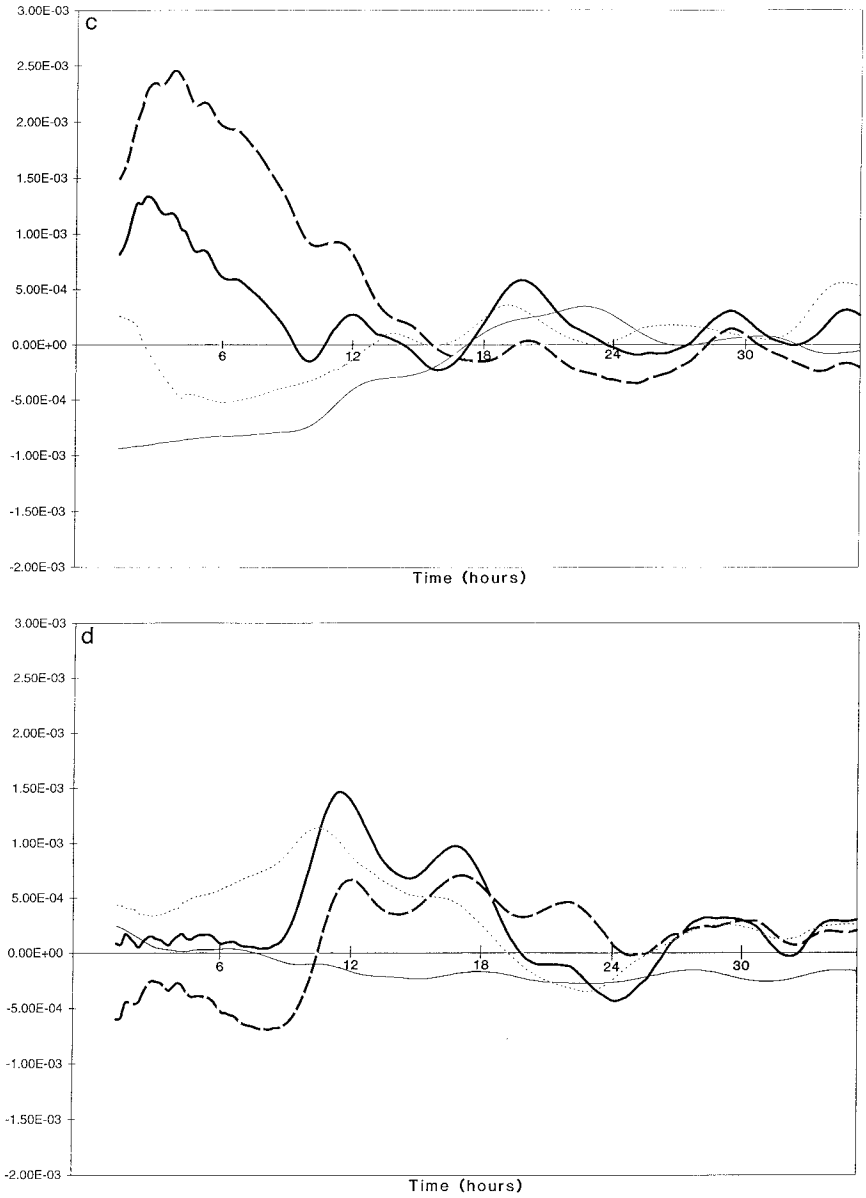

FIG. 21. (*Continued*)

cloud-filled boundary layer to the south and the shallow, stable boundary layer to the north. This indicates that cooler, more dense fluid from the south is displacing warmer, less dense fluid to the north. Ascending motion over the CTWR combined with descent ahead of the flow reversal has the effect of warming and suppressing the boundary layer to the north while cooling and deepening the boundary layer to the south (see Fig. 7).

A cross section of wind and potential temperature normal to the coast south of Monterey valid at 2200 UTC 10 June is shown in Fig. 20a. The cloud liquid water mixing ratio and potential temperature are shown in Fig. 20b. This plane, which is indicated by *CD* in Fig. 1, passes through the core of the low-level jet and is nearly the same plane as shown in Ralph et al. (1995) constructed from aircraft data. Only the component of the wind normal to the cross section plane is shown, such that positive values are for south-southeasterly winds and negative values indicate wind from the north-northwest. Although the depth and temperature of the MBL, the location of the jet core with respect to the inversion, and the location and extent of low clouds/fog are all in agreement with the aircraft observations, the strength of the inversion and the jet are significantly underforecast by the model. As the wind direction changes substantially over the plane, the maximum value of the normal component is very sensitive to small changes in the orientation of the plane (the maximum

value of the total wind speed in this plane at this time is 9 m s^{-1}). Near the coast, fanning of the inversion occurs (elevation of the upper part of the inversion and lowering of the lower part), consistent with that shown in the aircraft cross section.

In a cross section of potential temperature and cloud water parallel to the coast at hour 30 (not shown), the boundary layer depth is less than 100 m to the north and nearly 200 m within the cloudy region. This is consistent with the greater boundary layer depth following the passage of the CTWR shown in Figs. 19a and 19b. At this time, a continuous band of high liquid water content fog extends along the coast from north of Monterey Bay to south of San Miguel Island.

c. Momentum budget

To more closely examine the dynamics of the flow field, time series were constructed for terms of the horizontal momentum equations:

$$\frac{du}{dt} = fv - \frac{1}{\rho}\frac{\partial p}{\partial x} - D_x = f(v - v_g) - D_x \qquad (1)$$

and

$$\frac{dv}{dt} = -fu - \frac{1}{\rho}\frac{\partial p}{\partial y} - D_y = -f(u - u_g) - D_y, \qquad (2)$$

where

$$v_g = \frac{1}{f\rho}\frac{\partial p}{\partial x}, \qquad u_g = -\frac{1}{f\rho}\frac{\partial p}{\partial y},$$

$$\frac{d}{dt} = \frac{\partial}{\partial t} + u\frac{\partial}{\partial x} + v\frac{\partial}{\partial y} + w\frac{\partial}{\partial z},$$

and where u and v are the across-coast and along-coast components of the wind, respectively; f is the Coriolis parameter; ρ is the density; and $D_{x,y}$ represent the effect of horizontal diffusion and vertical turbulent mixing of momentum. The terms of Eqs. (1) and (2) are evaluated within the marine boundary layer at points *E* and *F* in Fig. 1 at an altitude of 55 m. Analysis of the time series at point *E* reveals the dynamics of the northwesterly flow regime, and the analysis at point *F* examines changes in the budget due to passage of the CTWR.

Shown in Fig. 21a are the time series of the components of the cross-coast momentum budget [Eq. (1)] at point *E*. At this location (near Pt. Reyes), the budget is dominated by the pressure gradient (heavy dashed line) and the Coriolis (light solid line). Thus, while the cross-coast momentum is approaching geostrophic balance, there is significant acceleration (heavy solid line) for a large portion of the forecast in the positive (westerly) direction. The sum of the horizontal diffusion and the vertical turbulent flux divergence (dotted line) is dominated by the latter, which opposes the acceleration and is largest when the acceleration is strong. A large diurnal variation is apparent in all of the terms in that the pressure gradient, Coriolis term, and the imbalance between them are largest during the time of the maximum coastal baroclinicity.

Figure 21b shows the time series of the components of the along-coast momentum budget [Eq. (2)] at the same location. Here, the dominant terms are the pressure gradient and the diffusion, indicating a quasi-antitriptic balance, although the acceleration is large in the positive (southerly) direction. Thus, the northerly component of the flow at this location is decelerating due to turbulent diffusion of momentum. The along-coast pressure gradient decreases in magnitude nearly monotonically for the first 24 h and then increases. This is consistent with Figs. 5, 8, 13, 14, and 18, which show a steady decrease in the pressure gradient over the first 24 h followed by an increase at hour 36.

Immediately downwind of point *E*, the flow decelerates and the onshore (westerly) component increases (Fig. 17). This is consistent with the accelerations shown in Figs. 21a and 21b, where the deceleration in v is generally stronger than the acceleration in u.

Terms of the momentum budget were also evaluated at an elevation of 410 m, well above the top of the marine boundary layer but below the terrain height. At this elevation, the diffusion is negligible and the balance in the across-coast momentum is similar to that at 55 m. The balance in the along-coast momentum is quite different from that at 55 m, however, as it is dominated by the pressure gradient and Coriolis terms. Thus, the quasi-antitriptic balance at 55 m is replaced by a more geostrophic flow at 410 m.

Figure 21c shows time series of the components of the across-coast momentum budget [Eq. (1)] at point *F* (south of Pt. Sur). While the balance is approaching geostrophic at this location, the dynamics and temporal evolution are considerably more complicated. Initially, the dominant terms are the pressure gradient and Coriolis but there is a large imbalance in that the pressure gradient is greater than the Coriolis by a factor of 1.5 (the large pressure gradient is due to coastal baroclinicity, just as at point *E*). Thus, $v_g > v$ and the acceleration decreases [Eq. (1)]. The across-coast component changes sign from easterly (offshore) to westerly (onshore) at hour 8 under the influence of strong acceleration resulting from this imbalance. Onshore flow, blocked by the terrain, contributes to ridging along the immediate coastline and leads to the rapid decrease and sign change in the pressure gradient at hour 16. The Coriolis term changes sign at hour 18 when southerly flow begins at this location. Following the transition to southerly flow, the pressure gradient and Coriolis are in opposition and these terms are much smaller than they were prior to hour 18.

Figure 21d shows time series of the components of the along-coast momentum budget [Eq. (2)] at point *F*. Initially, the along-coast flow is northerly and the dominant terms are the pressure gradient and diffusion, just as at point *E*. The pressure gradient begins to change

rapidly as a small-scale (~75-km diameter) low forms to the south of point *F* at hour 9 under the influence of offshore, downslope flow in the lee of the high terrain near Pt. Sur. It then propagates to the north into Monterey Bay by hour 13. With the formation of the low just to the south of point *F* the pressure gradient decreases slightly and then rapidly increases toward zero and the low encompasses point *F*. The pressure gradient then increases in the positive sense as the low moves toward the north.[1] The acceleration responds to the change in the pressure gradient and increases to a maximum at hour 12. The northerly flow is thus strongly decelerated (see the Coriolis term in Fig. 21c) and changes sign at hour 17. During the period from 18 to 24 h, the pressure gradient and Coriolis terms [$f(u - u_g)$] are nearly constant with $u_g > u$. The diffusion term leads to a reduction in the acceleration. The pressure gradient exhibits a periodic behavior with a period of approximately 6 h. This periodicity is even more apparent at the 410-m level (not shown).

At this location, three distinct phases can be seen in the along-coast momentum balance. Initially (from hour 0 to 8), the acceleration is small and the balance is near antitriptic (much as it is at point *E* for the entire 36 h). In the next phase (from hour 8 to 24; following the transition of the across-coast momentum from easterly to westerly), the momentum is unbalanced and the acceleration is the largest term as the pressure gradient and the flow transition from northerly to southerly. The most dramatic period of this phase is the first three hours when the pressure gradient rapidly changes sign, creating positive (southerly) acceleration. During the final phase, the along-coast momentum approaches a geostrophic balance, although the acceleration is of the same magnitude as the pressure gradient. This implies that the mass field is adjusting to the wind field as the low develops off Pt. Conception and the mesoscale ridge along the coast strengthens.

5. Impact of terrain on the CTWR

To clarify the impact of the terrain along the coast in blocking flow, several sensitivity studies were conducted in which the coastal geography and terrain field were simplified so as to eliminate variations in terrain height along the coast, breaks in coastal terrain, and bends in the coastline. In the first sensitivity study, the cross section of the terrain through the Santa Lucia Mountains and Coast Range south of Monterey Bay is broadcast along the coast producing a uniform 840-m-high ridge parallel to the straightened coastline from Pt. Conception to Pt. Reyes (Fig. 22). This results in a slight

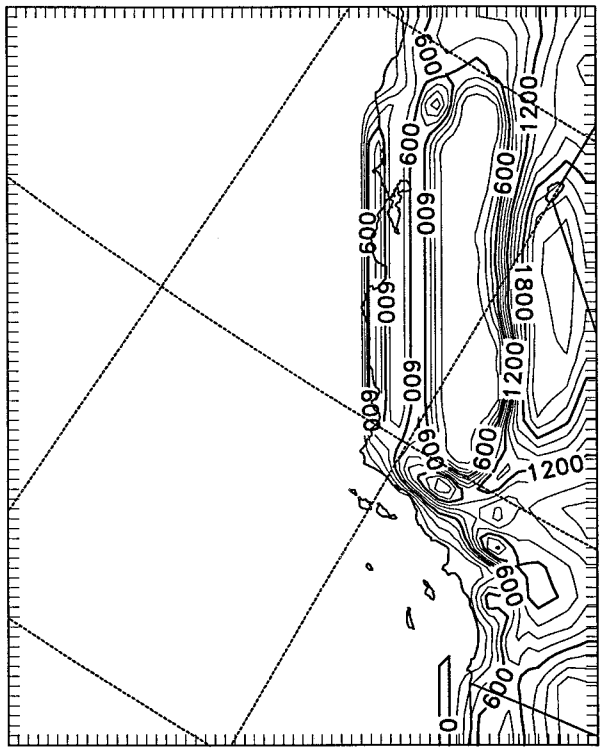

FIG. 22. Terrain height field (m) for the first sensitivity study. Contour interval is 150 m.

increase in the number of land points from the Monterey Peninsula to Pt. Reyes and south of Pt. Piedras Blancas (the coast near Big Sur is nearly unchanged). The new land points have surface roughness and temperature characteristics of adjacent coastal points. In a second sensitivity study, the same coastal geometry is used but the height of the coastal ridge is set to near 0. Each of the sensitivity simulations is initialized at 0000 UTC 10 June 1994 using the initial conditions from the control.

At 0600 UTC in the first sensitivity study, the 6-h forecast wind field shows uniform downslope flow along the entire ridge, resulting in warming over an approximately 1-km-deep layer centered at about 700 m and a slight reduction in SLP along the immediate coastline as compared to the control simulation. A cross section at hour 6 in the same plane as in Fig. 19 (not shown) indicates that the nearly neutral layer discussed above is deeper and warmer than in the control simulation. The minimum pressure along the coast extends nearly the entire length of the ridge; thus, there is no significant along-shore pressure gradient at this time. At hour 12, as at hour 6, the pressure minimum extends along nearly the entire coast and has decreased by 0.6 mb. A mesoscale pressure ridge is apparent in the southern California Bight.

Shown in Fig. 23a is the difference in forecast SLP between the control and the first sensitivity study at 1800 UTC (control minus sensitivity; less than zero indicates higher pressure in the sensitivity study). At this time,

[1] The small-scale low plays an important role at this location; however, the CTWR is a response to a larger mesoscale pressure gradient reversal extending initially from Pt. Conception to Pt. Sur and eventually to Pt. Reyes.

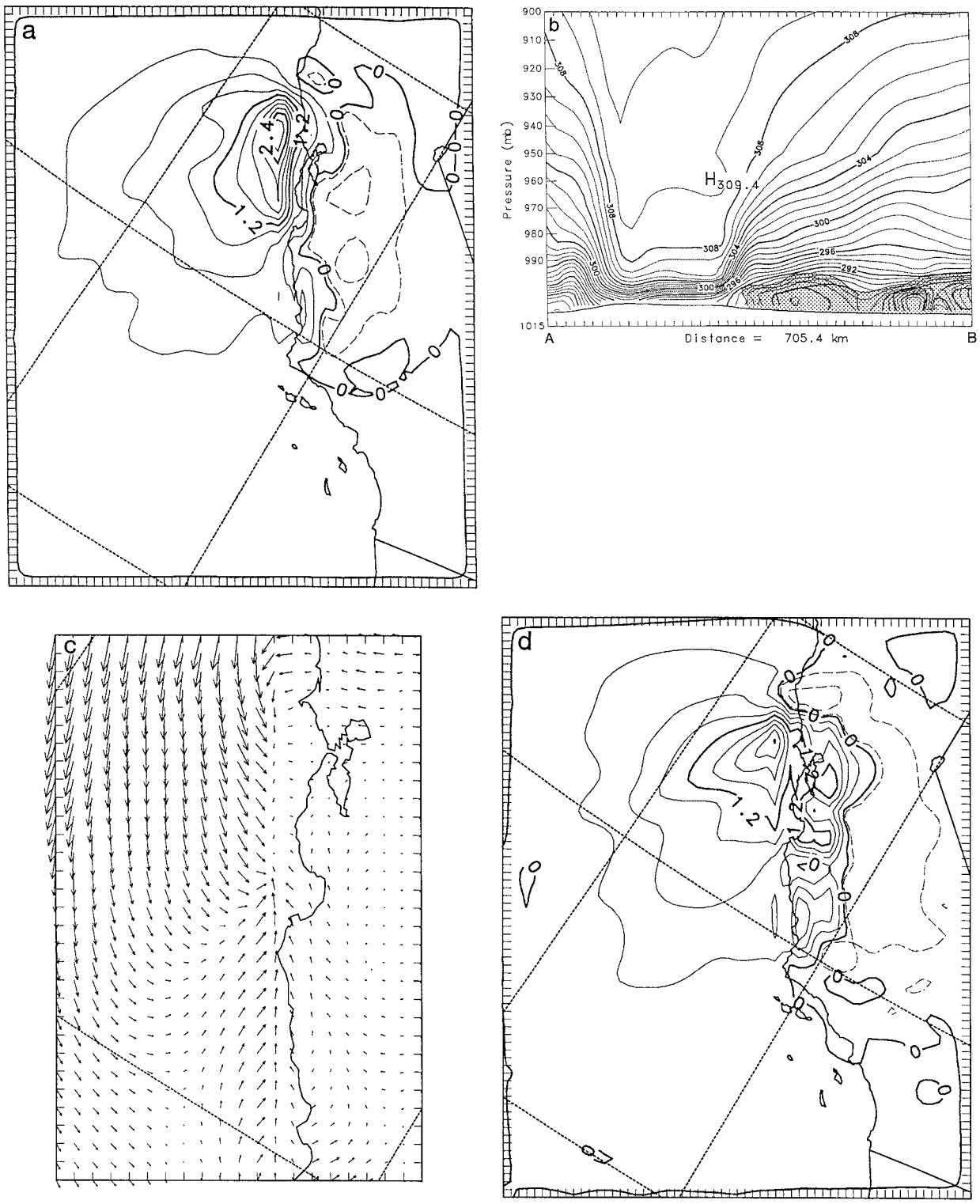

FIG. 23. Model fields from the first sensitivity study. (a) The 18-h forecast SLP difference (mb) (control run minus first sensitivity study) valid 1800 UTC 10 June 1994. Contour interval is 0.3 mb. (b) Model forecast cross section valid at 1800 UTC 10 June of potential temperature (K) and cloud liquid water mixing ratio (shaded). The plane of the cross section, *AB*, is shown in Fig. 1. Contour interval is 1 K. (c) The 18-h forecast 10-m wind vectors (m s^{-1}) valid 1800 UTC 10 June 1994. The largest wind vectors correspond to 20 m s^{-1}. (d) The 24-h forecast sea level pressure difference (mb) (control run minus first sensitivity study) valid 0000 UTC 11 June 1994. Contour interval is 0.3 mb. (e) The 24-h forecast 10-m wind vectors (m s^{-1}) valid 0000 UTC 11 June 1994. The largest wind vectors correspond to 20 m s^{-1}. (f) The 18-h forecast 950-mb vertical motion field (m s^{-1}) valid 1800 UTC 10 June 1994. Contour interval is 0.02 m s^{-1}.

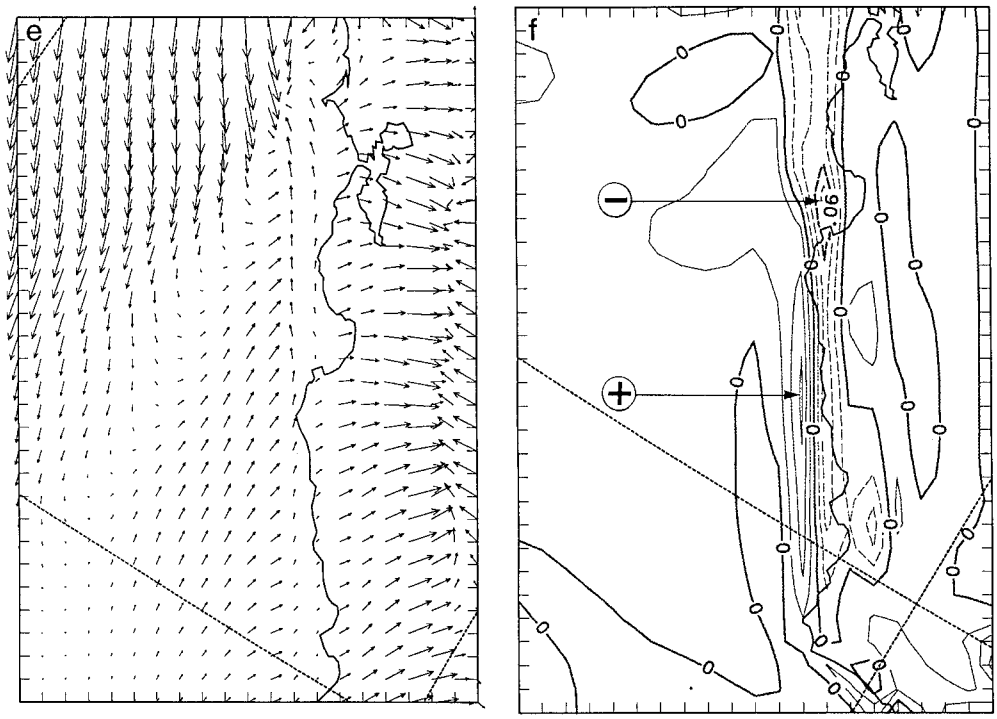

FIG. 23. (*Continued*)

the pressure gradient along the coast strengthens dramatically in the sensitivity study as the minimum pressure near Pt. Reyes decreases to 1007 mb (3 mb lower than in the control) while the pressure south of Pt. Piedras Blancas increases to 1011 mb. The minimum pressure is also farther to the north in this case (near Pt. Reyes as opposed to near San Francisco Bay in the control).

Lower pressure in the sensitivity study is a result of enhanced lee troughing; offshore flow north of San Francisco Bay localizes the largest pressure falls to the vicinity of Pt. Reyes. The extension of the 840-m-high ridge to north of Pt. Reyes leads to downslope flow of 0.10 m s^{-1}, which results in heating. Shown in Fig. 23b is a cross section of potential temperature at 1800 UTC 10 June from the sensitivity study from the same plane as shown in Fig. 19b. Note the suppressed boundary layer in the vicinity of Pt. Reyes that differs significantly from the control. During the period from 1200 to 1800 UTC in the control, cold advection (increasing from -1 K h^{-1} at 1400 UTC to -2 K h^{-1} at 1700 UTC) over the layer from about 200 to 800 m leads to an increase in SLP over coastal waters in the region near and to the north of Pt. Reyes. Over the same period in the sensitivity study, downslope adiabatic heating offsets cold advection and inhibits the destabilization seen in the control. The strength of the downslope flow is due to northeasterly flow at ridge-top level. South of Pt. Reyes, flow at ridge-top level is weakly onshore. At the surface, southerly flow develops along the coast to the latitude of Monterey Bay (Fig. 23c).

At hour 24, the minimum pressure (1007 mb) is just north of Pt. Reyes and the alongshore gradient remains strong. The primary feature of the pressure difference field (shown in Fig. 23d) is a lobe of lower pressure along the coast in the sensitivity study in an elongated region extending from north of Pt. Reyes to Santa Cruz. The largest pressure difference is 2.4 mb. Southerly flow extends to Pt. Reyes (Fig. 23e), well beyond the northerly extent in the control simulation (Fig. 12). The low clouds/fog extend nearly to the latitude of San Francisco Bay by hour 24. The alongshore gradient weakens at hour 30 and reintensifies at hour 36 as the pressure minimum moves to the south, reaching the latitude of San Francisco Bay by hour 36.

In this sensitivity test, the sea breeze is nearly eliminated by the 840-m-high ridge adjacent to the coast, although diurnal forcing results in ascending motion along the terrain in the afternoon. The CTWR propagates up the coast at an average speed of 11.7 m s^{-1} in the absence of the sea breeze. Moreover, with the influence of gaps in the coastal terrain and bends in the coastline removed, the northerly extent of the CTWR is determined entirely by the location of the pressure minimum—that is, the location at which the pressure gradient reverses.

Farther to the south, the vertical motion field at 950 mb shows a discontinuity associated with the CTWR. This is most pronounced at hour 18 (Fig. 23f). Along the coast north of Monterey Bay, a relatively uniform band of subsidence forms parallel to the ridge. At the northern boundary of the southerly flow (just south of

Monterey Bay), the band of subsidence shifts to the east and is replaced by ascending motion over the southerly flow. As in the control simulation, this vertical motion field has the effect of warming, stabilizing, and suppressing the boundary layer to the north while cooling and deepening the boundary layer to the south. Thus, the gradient in density across the leading edge of the southerly flow increases with time. Time animation of cross sections of potential temperature in a plane parallel to the coast shows the 100–200-m-deep cool boundary layer to the south moving north and displacing the warmer, less dense air to the north.

The results of the second sensitivity study, in which the same coastal geometry is used but the idealized 840-m-high coastal ridge is removed, are very different from those for the first sensitivity study. In this simulation, removal of the blocking terrain eliminates the CTWR. Southerly flow does occur due to large-scale quasi-geostrophic forcing (see section 3a), but there is no evidence of any mesoscale organization.

A cross section of potential temperature at 1800 UTC in the same plane as Fig. 19 is shown in Fig. 24a. Comparison of Fig. 24a to Fig. 19b for the control shows dramatic differences in the characteristics of the boundary layer. Note that the strong inversion over the northern coast shown in Fig. 19b is absent in this sensitivity study and that the depth of the boundary layer to the south is greater in Fig. 24a. The strength of the inversion over the central portion of the cross section is actually greater in this case due to offshore flow of the warm, continental boundary layer (unobstructed by terrain) above the cool marine air near the coast. The large horizontal gradients in potential temperature and boundary layer depth, indicative of an along-coast density gradient, are absent in the sensitive study results.

At 1800 UTC the flow is predominantly onshore as shown in Fig. 24b in contrast to the coast-parallel southerly flow in the control at this time. The SLP field is remarkably similar to the control. At hour 24, the flow is again predominantly onshore, although there is a small southerly component along the coast from Pt. Conception to Pt. Piedras Blancas. The SLP field is quite different from that in the control due to a 1-mb increase in the pressure along the coast and extending into the southern San Joaquin Valley. Higher pressure inland is the result of cooling due to onshore flow. At hour 36, the alongshore pressure gradient strengthens as a mesoscale trough develops. The mesoscale trough is similar to that in the control simulation at this time, although it is not as sharp and is much further to the south (extending from near Pt. Santa Cruz).

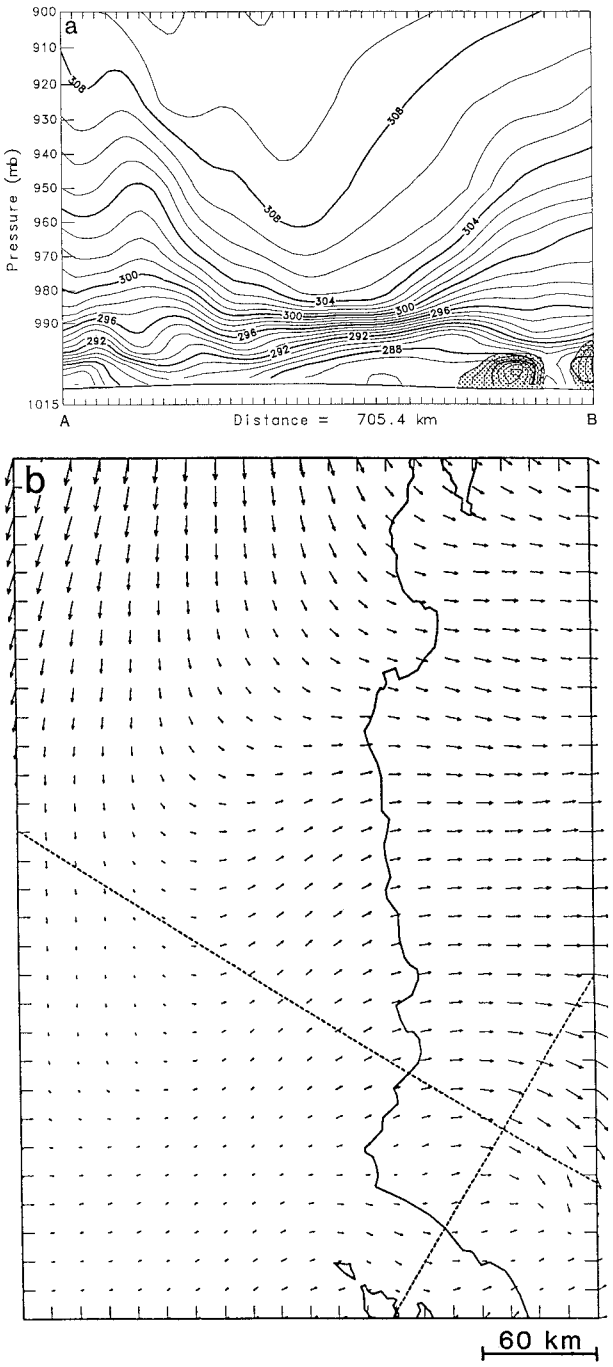

FIG. 24. Model fields from the second sensitivity study: (a) as in Fig. 23b but for the second sensitivity study, (b) 18-h forecast 10-m wind field valid 1800 UTC 10 June 1994. The largest wind vectors correspond to 10 m s^{-1}.

6. Discussion and concluding remarks

As demonstrated in section 4, the model performed well in simulating the 10–11 June 1994 event. The model reproduced many of the observed features, including the northward propagation of southerly flow in advance of a tongue of coastal stratus/fog along the coast; the anomalous vertical structure involving the relatively shallow boundary layer with the warm, nearly neutral layer above; the southerly low-level jet; and the substantial reduction in propagation speed due to the sea breeze. Certain discrepancies are apparent, however, in

that the southerly flow does not extend as far to the north and the offshore low is weaker.

The sensitivity studies clearly demonstrate the impact of coastal terrain on the CTWR. The results of the first sensitivity study show that the northerly extent of the southerly flow (see Figs. 12 and 23e) is determined by the location at which the along-coast pressure gradient reverses (the location of the minimum pressure). This is a result of lee troughing associated with offshore flow north of San Francisco Bay that localizes the strongest pressure falls, as suggested by MA87 and Mass and Bond (1996). In the control simulation, variations in coastal topography diminish this effect. The second sensitivity study shows that coastal terrain is required to produce the mesoscale organization associated with the CTWR. In this case, the large north–south gradient in density along the coast is absent (see Figs. 19b and 24a).

Analysis of the momentum budget at a level within the marine boundary layer (Figs. 21a–d) reveals much about the dynamics of this event. At a location north of Pt. Reyes in the northerly flow regime, the large along-coast momentum component is in near antitriptic balance as the northerly flow is decelerated by turbulent diffusion while the smaller across-coast momentum component is approaching geostrophic balance. At a location south of Pt. Sur, similar balances exist for the first 6–7 h. The across-coast momentum changes sign from easterly to westerly at hour 8. Blocking by the terrain results in a reversal in the across-coast pressure gradient at hour 16. With the establishment of southerly flow, the Coriolis term changes sign at hour 17 and the across-coast balance once again approaches geostrophy. In the along-coast component, three distinct regimes are apparent. Initially, the balance is near antitriptic until hour 8. From hours 8 to 24, large imbalances occur as both the along-coast pressure gradient and direction of the flow change sign. Following hour 24, the balance approaches geostrophic (although there is still significant acceleration) as the mass field adjusts to the wind field.

It is significant that the simulated CTWR displays features of several of the mechanisms proposed in the literature as described in the introduction above. This is, perhaps, not surprising; as noted by Ralph et al. (1996), the shallow MBL adjacent to steep coastal terrain can support a variety of propagating disturbances. The results of the control and first sensitivity study clearly indicate that pressure falls to the north play an important role. This is characteristic of the ageostrophic mesoscale response to an along-coast pressure gradient. The width of the southerly flow, which is near the Rossby radius of deformation (see Fig. 10), is also consistent with this mechanism. However, the results also show that processes operating on a much smaller scale (e.g., boundary layer processes) play an important role as well. The existence of a propagating mode suggests that, while the ageostrophic response to an along-coast pressure gradient may initiate southerly flow, other mechanisms are involved in the evolution of the CTWR.

The Kelvin wave mechanism requires a localized region of enhanced boundary layer depth propagating along the coast. After the passage of the Kelvin wave, boundary layer depth relaxes to its undisturbed state. This is not consistent with the results, which show that the boundary layer depth does not decrease after passage of the CTWR; in fact, the boundary layer depth increases monotonically to the south during the propagating phase. In contrast to the Kelvin wave dynamics, the results also show that the layer above the boundary layer is quite active and has a direct influence on the height of the MBL (see Figs. 19a and 19b).

The simulated CTWR has many features in common with a topographically trapped gravity current, particularly after approximately 1500 UTC 10 June. Chief among these is the apparent large gradient in density across the leading edge of the southerly flow with a deeper, cool boundary layer to the south and a shallow, stable layer to the north (see Fig. 19b). The concentration of the pressure gradient as the mesoscale ridge moves north along the coast is also consistent with this interpretation. Another common feature is the discontinuity in vertical motion across the leading edge, which forces, to some extent, the density gradient. Both of these features are more evident in the first sensitivity test than in the control.

An important feature of the gravity current is that the flow within the core of the current is generally close to the phase speed with which the gravity current propagates. Ralph et al. (1996) estimated the phase speed as 10–11 m s^{-1} using three coastal buoys from Pt. Conception to Monterey Bay. A relatively crude calculation of the flow reversal phase speed from the control simulation yields an average value of 11 m s^{-1} in close agreement. A more accurate estimate of the phase speed of the flow reversal is obtained from a determination of the time of flow reversal at the surface at a number of uniformly spaced ($\sim$40 km apart) points along the central coast. This analysis reveals two distinct propagation regimes in the model simulation. South of Pt. Piedras Blancas, where the coastal terrain is relatively low, flow reversal proceeds at 15 m s^{-1}, much faster than observed and much faster than the speed of the southerly flow in this region ($\sim$4 m s^{-1}). North of Pt. Piedras Blancas, where the coastal terrain forms a ''wall'' along the coast, flow reversal propagates at 6.9 m s^{-1}, more slowly than observed but in good agreement with the speed of the southerly flow in this region ($\sim$7 m s^{-1}). Thus, along this portion of the coast, the model results are consistent with the gravity current interpretation.

The model gives temporally and spatially continuous fields of important parameters, as well as showing propagation of various features. The ability to perform sensitivity studies shows the importance of distinct physical processes. Identification of these processes can be used to ''target'' observations to specific parameters and lo-

cations in future field studies. For example, the results suggest that vertical profiles of temperature and wind at several closely spaced points along the Santa Lucia mountain range just offshore would be useful in documenting structural changes not only in the boundary layer but also in the layer above and the existence (or absence) of an along-coast gradient in density. High spatial resolution along the coast would also be useful in documenting propagation (or the lack thereof).

In the future, we plan to conduct further studies to test the hypothesis that the CTWR is primarily a manifestation of a topographically trapped gravity current. We also plan to continue to investigate the dynamics of this and other more recent CTWR events.

Acknowledgments. We acknowledge the support of the sponsor, Office of Naval Research, and the program manager, Naval Research Laboratory, under program element 0602435N. The authors benefited from discussion of this work with several individuals, including Wendell Nuss and Paul Hirschberg of the Naval Postgraduate School, P. Ola G. Persson of the Cooperative Institute for Research in Environmental Science and the National Oceanic and Atmospheric Administration, and F. Martin Ralph and Melvyn A. Shapiro of the National Oceanic and Atmospheric Administration Environmental Technology Laboratory. We also thank the anonymous reviewers whose comments helped to improve the manuscript. The assistance of Steven Bishop of the Naval Research Laboratory in drafting some of the figures is acknowledged.

REFERENCES

Blackadar, A. K., 1962: The vertical distribution of wind and turbulent exchange in a neutral atmosphere. *J. Geophys Res.,* **67,** 3095–3103.

Bond, N. A., C. F. Mass, and J. E. Overland, 1996: Coastally trapped wind reversals along the United States west coast during the warm season. Part I: Climatology and temporal evolution. *Mon. Wea. Rev.,* **124,** 430–445.

Businger, J. A., J. C. Wyngaard, Y. Izumi, and E. F. Bradley, 1971: Flux profile relationships in the atmospheric surface layer. *J. Atmos. Sci.,* **28,** 181–189.

Deardorff, J. W., 1978: Efficient prediction of ground surface temperature and moisture, with inclusion of a layer of vegetation. *J. Geophys Res.,* **83,** 1889–1903.

Dorman, C. E., 1985: Evidence of Kelvin waves in California's marine layer and related eddy generation. *Mon. Wea. Rev.,* **113,** 827–839.

——, 1987: Possible role of gravity currents in northern California's coastal summer wind reversals. *J. Geophys. Res.,* **92,** 1497–1506.

Harshvardhan, R. Davies, D. A. Randall, and T. G. Corsetti, 1987: A fast radiation parameterization for atmospheric models. *J. Geophys. Res.,* **92,** 1009–1016.

Hodur, R. M., 1997: The U. S. Navy's coupled ocean/atmosphere model (COAMPS). *Mon. Wea. Rev.,* **125**, 1414–1430.

Hogan, T. F., and T. E. Rosmond, 1991: The description of the Navy Operational Global Atmospheric Prediction System's spectral forecast model. *Mon. Wea. Rev.,* **119,** 1786–1815.

Klemp, J., and R. Wilhelmson, 1978: The simulation of three-dimensional convective storm dynamics. *J. Atmos. Sci.,* **35,** 1070–1096.

——, R. Rotunno, and W. C. Skamrock, 1994: Propagation of atmospheric gravity currents along a coastal barrier. Preprints, *Sixth Conf. on Mesoscale Processes,* Portland, OR, Amer. Meteor. Soc., 497–500.

Louis, J.-F., 1979: A parametric model of vertical eddy fluxes in the atmosphere. *Bound.-Layer Meteor.,* **17,** 187–202.

Mass, C. F., and M. D. Albright, 1987: Coastal southerlies and alongshore surges of the west coast of North America: Evidence of mesoscale topographically trapped response to synoptic forcing. *Mon. Wea. Rev.,* **115,** 1707–1738.

——— and ———, 1989: Origin of the Catalina Eddy. *Mon. Wea. Rev.,* **117**, 2602–2436.

——— and N. A. Bond, 1996: Coastally trapped wind reversals along the United States West Coast during the warm season. Part II: Synoptic evolution. *Mon. Wea. Rev.*, **124**, 446–461.

———, ———, and D. J. Brees, 1986: The onshore surge of marine air into the Pacific Northwest: A coastal region of complex terrain. *Mon. Wea. Rev.* **114**, 2602–2627.

Mellor, G. L., and T. Yamada, 1982: Development of a turbulence closure for geophysical fluid problems. *Rev. Geophys. Space Phys.,* **20,** 851–875.

Oosterling, P. S., 1995: Coastally trapped disturbances along the U. S. west coast: Synoptic and mesoscale analysis of 9–12 June 1994. M. S. thesis, Naval Postgraduate School, Monterey, CA, 73 pp. [Available from Department of Meteorology, Naval Postgraduate School, Monterey, CA 93043-5000.]

Persson, P. O. G., P. J. Neiman, and F. M. Ralph, 1995: Topographically generated potential voricity anonolies: A proposed mechanism for initiating coastally trapped disturbances. Preprints, *Seventh Conf. on Mountain Meteorology*, Breckenridge, CO, Amer. Meteor. Soc., 216–222.

——, ——, and ——, 1996: The role of a topographically generated potential vorticity anomaly in initiating a coastal wind reversal. Preprints, *Conf. on Coastal Oceanic and Atmospheric Prediction,* Atlanta, GA, Amer. Meteor. Soc., 120–124.

Ralph, F. M., P. J. Neiman, P. O. G. Persson, W. D. Neff, J. Miletta, L. Armi, and J. M. Bane, 1995: Observations of an orographically trapped disturbance along the California Coast on 10–11 June 1994. Preprints, *Seventh Conf. on Mountain Meteorology*, Breckenridge, CO, Amer. Meteor. Soc., 204–211.

——, ——, ——, W. Nuss, C. Dorman, and W. D. Neff, 1996: The evolution of a coastally trapped atmospheric disturbance along the California Coast on 10–11 June 1994. Preprints, *Conf. on Coastal Oceanic and Atmospheric Prediction*, Atlanta, GA, Amer. Meteor. Soc., 129–135.

Reason, C. J. C., and D. G. Steyn, 1992: The dynamics of coastally trapped mesoscale ridges in the lower atmosphere. *J. Atmos. Sci.,* **49,** 1677–1692.

Rogerson, A. M., and R. M. Samelson, 1995: Synoptic forcing of coastal-trapped disturbances in the marine atmospheric boundary layer. *J. Atmos. Sci.,* **52,** 2025–2040.

Rutlidge, S. A., and P. V. Hobbs, 1983: The mesoscale and microscale structure and organization of clouds and precipitation in midlatitude cyclones. VIII: A model for the ''seeder-feeder'' process in warm-frontal rainbands. *J. Atmos. Sci.,* **40,** 1185–1206.

Smagorinsky, J., 1963: General circulation experiments with the primitive equations. I. The basic experiment. *Mon. Wea. Rev.,* **91,** 99–164.

Therry, G., and T. LaCarr're, 1983: Improving the eddy kinetic energy model for the planetary boundary layer description. *Bound.-Layer Meteor.,* **25,** 63–88.

Thompson, W. T., and S. D. Burk, 1991: An investigation of an Arctic front with a vertically nested mesoscale model. *Mon. Wea. Rev.,* **119,** 233–261.